HAL
open science

Carbon black/electrolyte interface study by electromagnetic and electrochemical techniques in γAl2O3/poly(vinylidene fluoride)/carbon black composite materials: Application for lithium-ion batteries

Nicolas Gauthier, Anshuman Agrawal, Olivier Dubrunfaut, Sylvain Franger, Bernard Lestriez, Jean-Claude Badot, Loïc Assaud

To cite this version:

Nicolas Gauthier, Anshuman Agrawal, Olivier Dubrunfaut, Sylvain Franger, Bernard Lestriez, et al.. Carbon black/electrolyte interface study by electromagnetic and electrochemical techniques in γAl2O3/poly(vinylidene fluoride)/carbon black composite materials: Application for lithium-ion batteries. Electrochimica Acta, 2023, 437, pp.141495. 10.1016/j.electacta.2022.141495 . hal-04001778

HAL Id: hal-04001778

https://hal.science/hal-04001778

Submitted on 7 Mar 2023

HAL is a multi-disciplinary open access archive for the deposit and dissemination of scientific research documents, whether they are published or not. The documents may come from teaching and research institutions in France or abroad, or from public or private research centers.

L'archive ouverte pluridisciplinaire **HAL**, est destinée au dépôt et à la diffusion de documents scientifiques de niveau recherche, publiés ou non, émanant des établissements d'enseignement et de recherche français ou étrangers, des laboratoires publics ou privés.

Carbon Black/Electrolyte Interface study by Electromagnetic and Electrochemical Techniques in γAl_2O_3/Poly(vinylidene fluoride)/Carbon Black Composite Materials: Application for Lithium-Ion Batteries

Nicolas Gauthier,[a,b] Anshuman Agrawal,[a,b,c] Olivier Dubrunfaut,[b] Sylvain Franger,[a] Bernard Lestriez,[d] Jean-Claude Badot,[c,e] and Loïc Assaud[a*]

[a] ICMMO-ERIEE, Université Paris-Saclay, UMR CNRS 8182, 17 avenue des Sciences, 91400 Orsay, France
[b] GeePs Group of electrical engineering - Paris, UMR CNRS 8507, CentraleSupélec, Sorbonne Université, Université Paris-Saclay, 11 rue Joliot-Curie, 91192 Gif-sur-Yvette, France
[c] Chimie ParisTech, Université PSL, , Institut de Recherche de Chimie Paris, UMR CNRS 8247, 11 rue P. et M. Curie, 75005 Paris, France
[d] Institut des Matériaux de Nantes Jean Rouxel, UMR CNRS 6502, Nantes Université, 2 rue de la Houssinière, BP32229, 44322 Nantes, France
[e] Réseau sur le Stockage Electrochimique de l'Energie (RS2E), FR CNRS 3459, France

*Corresponding Author loic.assaud@universite-paris-saclay.fr

Abstract

This work aims at better understanding the interactions existing between the liquid electrolyte and the solid composite electrode in a Li-ion battery. We substituted the common active material (e.g. $LiNi_{1/3}Mn_{1/3}Co_{1/3}O_2$ or $LiFePO_4$) by an insulating (inactive) γ-Al_2O_3 compound in order to detect and evidence the interaction between the carbon black electronic additive and the liquid electrolyte. Our study presents the characterization of charge (electrons and ions) transport at different scales by combining a high-frequency analysis performed by broadband dielectric spectroscopy (BDS, up to 10^{10} Hz), along with a low-frequency analysis performed by electrochemical impedance spectroscopy (EIS, down to 10^{-3} Hz). Two carbon black materials with two different specific surface areas (80 $m^2.g^{-1}$ and 65 $m^2.g^{-1}$, respectively) were studied. The electronic percolation threshold and the kinetics of impregnation of the hierarchical composite electrode by the liquid electrolyte have been determined with respect to the carbon black content. The significant influence of the adsorbtion of ions at the carbon black surface on the electrons transport is particularly highlighted and explained.

1. Introduction

Nowadays, Li-ion batteries are used for electrical energy storage in a wide set of applications such as electronic portable devices, hybrid vehicles and more recently full-electric vehicles.[1] Much effort has been devoted, in the last decade, to the development of new compounds, new architectures and new technologies[2] (e.g. Li-air, Na-ion, Li-S) and new electrolytes[3,4]. Among the various commercial electrochemical energy storage systems, Li-ion batteries exhibit the best performance today.[5] However, despite the significant benefits that Li-ion batteries offer as an energy storage system, the electrode processing technology suffers from limitations with regard to power and energy densities of the final product.[6] As a result, 50% of batteries weight and volume consist of non-electroactive parts (collectors, separators, electrolyte). The limitations mainly originate from altered charge transport in these complex multi- and hierarchical materials (Fig. 1).[7,8] In addition to the active material (AM), carbon black (CB) and polymeric binder (PB) are widely used as additives to enhance the electronic conduction and overall cohesion respectively within the electrode. Electronic and ionic conductivities are the two major parameters leading to good or poor electrochemical behaviour.[9,10] Up to now, most of the studies demonstrates that the rate limitations, for commercially available active materials, are mainly due to the electrode architecture and not to mass transport in the active materials. However, to date, only a few studies have reported on the direct measurement of the electrical properties (including both electronic and ionic charge transport of the electrode), from the macroscopic to the nanometric scales. In fact, regarding the electronic transport, the *dc* electronic conductivity (σ_{dc}) is most often the only parameter to be measured in the dry state (*ex situ*). σ_{dc} is a macroscopic averaged value that provides poor information on the real electrical transport properties, especially in powdered materials, such as composite electrodes, consisting of different individual particles and their clusters. Then, the particles are separated by resistive and capacitive barriers (e.g. cluster or particle boundaries), that limit the electronic transfer. Furthermore, only a few studies have tried to measure the *dc* electronic conductivity in the wet state, i.e. *impregnated electrode*.[6,11,12,13,14] One must also consider the role of interfaces (adsorption of ions to the surface of active material and carbon particles), and the subsequent physical interactions at these interfaces.[6,9,10] The conductivity of the wet electrode drops as compared to the dry electrode due to the nanometric size of the carbon black particles that leads to a particularly

high specific surface area. Indeed, due to surface effects, the adsorbed Li^+ cation and PF_6^- anion will modify the overall carbon black conductivity. Moreover, EC-DMC dipoles from the electrolyte and PvdF-HFP dipolar species interact more to one another. In a previous work, the active material was substituted by an insulating compound (γ-Al_2O_3) and studied by broadband dielectric spectroscopy (BDS) in order to understand only the interactions between the carbon black and the electrolyte. [6] Previous experimental data have revealed that the ion adsorption leads to a decrease of the electronic conductivity of the samples due to the existence of energy barriers contrary to the dry samples in which the electronic transfer can be achieved by tunneling.

In this report, we now focus on the electrolyte/carbon black interface study in a γAl_2O_3/Poly(vinylidene fluoride)-HFP/Carbon black composite material by using two types of carbon black powders with different specific surface areas. The electronic conductivity, for both dry and impregnated (by electrolyte) samples, was measured using broadband dielectric spectroscopy (BDS). Moreover, these measurements were combined with electrochemical impedance spectroscopy (EIS) in order to have access to the broadest range of frequencies, from GHz to mHz. These measurements allowed us i) to fundamentally understand the influence of the electrolyte ions adsorption on the conduction properties, ii) to determine the electronic percolation threshold with respect to the carbon black content and finally iii) to propose a model for kinetics impregnation of the composite solid electrode by the liquid electrolyte.

2. Experimental

2.1. Chemicals and sample preparation

Standard chemicals were used as received. Reactive gas (N_2 alpha 1), for porosity measurements, was supplied by Air Liquide. One of either two carbon black powders with differing specific surface areas of 80 $m^2.g^{-1}$ (denoted CB1) and 65 $m^2.g^{-1}$ (denoted CB2) was used as a conductive agent additive for each specific sample. CB1 was supplied by Alfa Aesar and CB2 (Super C65) by IMERYS Graphite & Carbon. Anhydrous γ-alumina was supplied by Merck and poly(vinylidene fluoride *co*-hexafluoropropylene) (PVdF-HFP) used as polymeric binder (PB) was supplied by ARKEMA (Kynar flex 2751-00). The composite mixture was produced in batches of 200 mg with the following compositions: i) 7 wt% of PB, ii) from 6.5 to 20 wt% of CB and (iii) γ-alumina, its content being readjusted to maintain the total mass

constant (200 mg). PB was first dissolved in 3 mL of acetone for 4 hours. A CB/γ-Al_2O_3 mixture was ground using a mortar and pestle and subsequently added to the solution. The mixture was then stirred magnetically overnight for 12 hours and subsequently evaporated on a heat-plate at 40°C. EIS and BDS studies were conducted with following carbon black loading:

a) for CB1: 8 wt% (i.e. volume fraction = 5.3 %), 10 wt% (i.e. volume fraction = 6.9 %), 12.5 wt% (i.e. volume fraction = 7.8 %) and 15 wt% (i.e. volume fraction = 9.2 %);

b) for CB2: 6.5 wt% (i.e. volume fraction = 4.5 %), 8 wt% (i.e. volume fraction = 5.3 %), 10 wt% (i.e. volume fraction = 6.9 %), 12.5 wt% (i.e. volume fraction = 7.8 %) and 15 wt% (i.e. volume fraction = 9.2 %).

The mean total porosity is 44 ± 3 % after densification (see below) and the amount of PVdF-HFP was kept unchanged at 7 wt% (i.e. volume fraction of 5.8 ± 0.3 %) for all the studied samples.

The concentrations of the various components will then be indicated in volume percent in the next sections.

2.2. Morphological and surface characterizations

The specific surface area of the composite material was determined using the Brunauer-Emmett-Teller (BET) method based on the measurement of N_2 gas adsorption/desorption isotherms, with a Belsorp II analyzer from BEL Japan Inc. The morphology of the composite electrode was characterized by scanning electron microscopy using a Zeiss FEG-SEM equipped with an in-lens detector.

2.3. Electrochemical impedance spectroscopy setup

Regarding the electrochemical impedance spectroscopy (EIS) measurements, the powdered γ-Al_2O_3/CB/PB mixture was trapped in a 13-mm diameter stainless-steel grid that served as a current collector. It was then calendered under a pressure of about 258 MPa to produce a pellet (*thickness =0.78-1.15 mm, diameter = 7 mm and weight ≈ 44-65 mg*). The resulting sample served as a working-electrode, whereas a lithium disk and a lithium rod were used as counter and reference electrodes, respectively. These three electrodes were assembled in an EL-cell (from BioLogic) with two layers of porous glass paper separator soaked with the aforementioned LP30 electrolyte. All cells assembling was carried out in a Jacomex glovebox (under controlled Ar atmosphere: O_2 < 1 ppm, H_2O < 1 ppm). EIS measurements were performed using a VMP3 system from BioLogic. The frequency range scanned was 10^{-3} to

5×10^4 Hz, with a sinusoidal perturbation voltage amplitude of 30 mV, and a cell voltage drift before experiment less than 1 mV.h^{-1}.

2.4. Broadband dielectric spectroscopy setup

Sample pellets of powdered γ-Al_2O_3/CB/PB (*thickness =0.65-0.85 mm, diameter = 7 mm and weight ≈37-48 mg*) were produced by applying a pressure of about 258 MPa to carry out BDS measurements. Complex conductivity and permittivity spectra were recorded over a broad frequency range (*from 10^6 to 10^{10} Hz for all measurements*), using both an Agilent 4294A impedance and a Keysight E8364B network analysers. The experimental device consisted of a coaxial cell (*APC7 standard*), for both dry and wet samples measurements, in which the cylindrical sample was coated in front and back side by a 200-nm gold film (*diameter: 3.04 mm and 7 mm, respectively*) and positioned between the coaxial waveguide and a short circuit *(see K.A. Seid et al. [9] for a complete description)*[15,16]. The relative complex permittivity $\varepsilon(\omega) = \varepsilon'(\omega) - i\varepsilon''(\omega)$ of the sample was obtained from its admittance Y_s. A LP30 solution (1 M $LiPF_6$ solution in an ethylene carbonate/dimethyl carbonate mixture (EC/DMC 1/1 w/w)) was used as the electrolyte for soaking the electrodes.

3. Results and discussion

3.1. Architecture of γ-Al_2O_3/CB/PVdF-HFP composite materials

The general morphology of the composite dry materials is shown in Figure 2. For different CB1 loadings, from 5.3 % to 9.2 % in volume fraction, the SEM micrographs revealed micro-sized clusters corresponding to alumina, homogeneously distributed along the surface of the electrode. CB1 is made of nanometric spherical particles of about 10 nm which constituted the smallest dispersible compounds. After processing, these particles are connected by chemical bonds to form linear agglomerates of 300-500 nm in diameter. Agglomerates of CB particles are visible, and hereafter denoted as clusters. These clusters are physically bonded together. The PB is deposited at the surface of the γ-Al_2O_3 and formed with the CB a continuous three-dimensional network that connected the different components of the composite electrode all-together. Similar morphology was observed for CB2-based composites. BET adsorption/desorption measurements (Figure 3) allowed the determination of the mesopores diameter, which for both CB-containing dry electrodes, was in the range of 2.4 nm. The specific surface areas of each CB used in the study were of 80 $m^2.g^{-1}$ and 65 $m^2.g^{-1}$ for CB1 and CB2, respectively. Note that CB2 is a highly conductive carbon, particularly

designed to be integrated in Li-ion battery electrodes, whereas CB1, exhibiting a larger specific surface area, is used for comparison, to evaluate the influence of the possible interactions at the electrolyte/CB interface. However, the SEM micrographs revealed the same geometry and morphology of the resulting composite dry electrode for both CB. SEM and adsorption/desorption analyses did not provide sufficient information, regarding the electrode architecture, with respect to its electrical properties at the nano-scale. The electronic contacts within the composite electrode are likely to be described as tunnel junctions. Indeed, a tiny variation in the gap thickness may make the difference between a conductive and non-conductive path. Moreover, at the microscale, the CB can only be seen as a network of clusters. Hence, it is difficult to obtain a quantitative description of the morphology and the geometry of the composite electrode, due to the dense, complex, and hierarchical structure of the different compounds. In the following sections, we focus on the correlation of the evolution of conductivity measured by electrochemical and electromagnetic techniques with respect to a change in the carbon black composition.

3.2. Electrochemical impedance spectroscopy

The wet electrodes were further characterized at lower frequencies (10^{-3} to 5×10^{4} Hz) by complex electrochemical impedance spectroscopy (EIS).[17,18,19] This technique is complementary to the broadband dielectric spectroscopy technique (see next section) since it allows the conductivity characterization at lower frequencies.[20,21] Figure 4 displays the Nyquist diagram of complex impedance Z normalized by the surface area of carbon black (*i.e. specific surface with respect to carbon black weight*) that is under study. Note that the EIS measurements were performed immediately after the electrodes being soaked by the electrolyte. Nyquist plots exhibit two main relaxation phenomena as shown in the equivalent circuit (Figure 5). No relaxation related to charge transfer (electrochemical kinetics) is expected here as neither the inactive alumina nor the carbon black exhibits any Li^{+} intercalation at the operating voltage applied (3.1 V vs. Li^{+}/Li).

To qualify the contact at the current collector/electrode interface, the areal density of contacts at the interface, Σ (*contact number by surface unit*) can be introduced. The contact resistance (*in* $\Omega.m^2$) is given as $R_C = R_{cr} + R_f$, where R_{cr} is the constriction resistance and R_f is the resistance of the native oxide film present at the extreme surface of the metallic current collector. R_f is not expected to vary with the electrode composition.[22,23] The constriction resistance R_{cr} expected to vary as:

$$R_{cr} \propto \frac{1}{\sigma_{dc} \times \Sigma} \quad (1)$$

where σ_{dc} is the global conductivity of the electrode.[24] No semi-circles were observed for all CB contents below 5.3%, corresponding to the lack of efficient electronic percolation. The total impedance recorded is so large (> 1 kΩ.m^2) that no accurate quantitative information could be extracted from these measurements. Beyond 5.3% of CB, the electronic percolation was clearly achieved, consistent with the results obtained in broadband dielectric spectroscopy measurements *(see § 3.3)*. A higher content in CB also leads to a lower corresponding impedance. Thus, electronic conduction increased with CB loading, also consistent with the BDS analysis *(see § 3.3)*.

In addition, the electronic percolation for CB1 was reached with a slightly smaller loading of carbon black. This could be related to the higher specific surface area of the corresponding carbon. Moreover, the relaxations at the lower frequencies exhibit larger resistances for CB1 *(i.e. 170-180 Ω.m^2)* than CB2 *(i.e. 60-70 Ω.m^2)* counterpart with the same CB loading 9.2%. Two assumptions would be considered to explain this phenomenon at the macroscopic scale (i.e. sample size), given the frequency band used in EIS. The first one could be assigned to larger resistances due to greater interactions (adsorption) between carbon and electrolyte, stemming from the higher surface exchange offered by the larger specific surface area of CB1. The second one would focus on the formation of a solid electrolyte interphase (SEI) which would passivate the carbon surface. This second hypothesis is only retained if the sample has remained in contact with the electrolyte for about a day. As the sample is soaked and measured right after, the SEI may possibly exist in very small amount. In both cases, this should give rise to an increase the contact resistance, and subsequently lowering the global conductivity.

The two relaxations observed experimentally and shown in Figure 5a were correlated with two inflexion points in the corresponding phase-Bode diagram (not shown here), reinforcing the assumption that two distinct phenomena are taking place. These two relaxations are thus modelled with an electrical equivalent circuit, consisting in two (*R//Q*) elements in series, *R* being a resistor, and *Q* a constant phase element (CPE), expressing the non-ideality of a capacitor ($Z_{CPE} = 1/Q(i\omega)^{\alpha}$). Two additional elements have been added: a resistance, R_{int}, containing a part of the aforementioned contact resistance, R_C, and the bulk liquid electrolyte resistance (finite ionic motion in the liquid phase), and an open Warburg

element *W*, for modelling the semi-infinite ionic diffusion (medium frequency straight line at 45° in Nyquist plot) and ions accumulation (low frequency capacitive behaviour at 90° in Nyquist plot) in the electrode vicinity (confined electrolyte). The corresponding equivalent circuit is displayed as inset in Figure 5a. For the CB contents of 6.9%, 7.8% and 9.2%, these ratios being chosen to ensure the electronic percolation), two contributions *R//Q* have been always distinguished (through the phase inflexion detection [25]) as shown in Figure 5b. R_1 denotes the resistance measured at high frequency, in the range of 5 kHz (1st relaxation), whereas R_2 denotes the resistance measured at lower frequency, in the range of 1 kHz (2nd relaxation). R_1 was lower for samples with more CB content. Conversely R_2 remains more constant as a function of time. Therefore, R_1 seemed to be more associated with the electronic conductivity. In particular, concerning the compositions of CB, 6.9% and 7.8%, the R_1 resistance decreases (from ~ 100 to 50 $\Omega.m^2$) with time during the three first days followed by a daily increase (~ 18 $\Omega.m^2.day^{-1}$). Actually, the R_1 first decrease may be attributed to the impregnation delay of the composite electrode by the liquid electrolyte, leading to an improvement of exchange surfaces within the materials. The subsequent increase could be attributed to a deterioration of the contacts, possibly from a cohesion loss between the various components of the electrodes, and the formation of agglomerates, associated with a decrease in active surface area. This phenomenon was not observed for the composition of CB 9.2%. In this latter case, R_1 resistance slightly increased (of about 3 $\Omega.m^2.day^{-1}$) all along the impregnation. This shows that a higher CB loading combined with a higher specific surface area seems to be less affected by the liquid electrolyte impregnation, maintaining a constant quality of contacts and exchange surfaces. Thus, R_1 contributes to the contact resistance, R_C especially through R_{cr} mainly associated with the grain-to-grain contact. On another hand, R_2 could be assigned to the formation of the solid electrolyte interphase (SEI) due to the passivation of the surface of the composite electrode by the liquid electrolyte degradation products (such as solvents, and inorganic salts). R_2 increases slightly, for the 2 lower CB loadings 6.9 and 7.8%, during the six first days of the study and then remained constant (~ 50 $\Omega.m^2$), whereas R_2 for the highest CB loading 9.2% is mostly constant since the beginning, at a much lower value (~ 10 $\Omega.m^2$). The stability of R_2 may be ascribed to the completion of the SEI formation, known to be obtained on carbon-based materials.[26] Due to its dielectric nature and location (surface thin film), R_2 may also contribute to the contact resistance, R_C. Thereafter, the determination of the real value of this contact resistance, R_C is very tricky, as

one can notice several contributions arising from different phenomena. Moreover, as previously shown, a change in the surface area and/or porosity of the solid phase is also responsible for noticeable changes in terms of exchange surface and passivation of the composite electrodes, making this determination very complex and fluctuant with time. However, it has been highlighted here that the choice of the carbon additive, the formulation (loading) and the wetting of the electrode are interdependent parameters, playing through the overall contact resistance, and SEI formation. Now considering the low frequencies (*i.e.* < 1 Hz), in the Nyquist plots, it can also be noticed (Figure 6a) that the semi-infinite diffusion domain (45° straight line) is function of both the CB content and the time of impregnation, but is less affected by the CB specific surface area (Figure 8). This is directly related to the architecture (porosity/tortuosity) of the composite electrodes, which obviously depends less on the carbon surface than on the carbon content and time (liquid electrolyte impregnation opens porosities). Actually, this domain refers to the confined electrolyte inside the vicinity of the composite electrode. When noticeable on the Nyquist plot, it means the porosities are opened and wide enough to ensure good ionic transport.[27]

According to the EIS measurements performed just after wetting the electrode and up to 22 consecutive days as presented on Figure 6, this domain slowly appears with 6.9% CB (only visible after 22 days), whereas it is already visible (after 1 day) with 9.2% CB. This is consistent with the mesoporosity of the dry electrodes, previously highlighted by BET. The amount of pores, proportional to the CB content, which can be filled by the liquid electrolyte will lead to a certain swelling of the electrode, enlarging the ionic diffusion pathways. That is why a protocol of electrode formation (shaping) is so important before cycling a Li-ion batteries to ensure good ulterior performance, especially for the ionic mass transport.

3.3. Broadband dielectric spectroscopy

The broadband dielectric spectroscopy (BDS) allows for the characterization of different types of polarization and charge carrier motion under the influence of an electromagnetic field across the sample, at different scales. This technique is mainly known for polymers and ionic conductive materials but has been less used for electronic conductive materials. When submitted to a time-dependent electric field $E(t)$, the electrical response of a material is due to charge density fluctuations. In a harmonic regime, the relationship between the frequency-dependent complex conductivity $\sigma(\omega) = \sigma'(\omega) + i\sigma''(\omega)$ and relative permittivity $\varepsilon(\omega) = \varepsilon'(\omega) - i\varepsilon''(\omega)$ is defined by:

$$\sigma(\omega) = \sigma_{dc} + i\omega\varepsilon_0\varepsilon(\omega) \quad (2)$$

where σ_{dc} is the macroscopic direct-current conductivity, ε_0 = 8.842×10^{-12} F.m^{-1} the vacuum permittivity and $\omega = 2\pi\nu$ the angular frequency (*ν being the frequency, expressed in Hz*).

In electronic conductors, several types of polarization occur, coming from the crystal structure, particle nanostructure and sample microstructure [5,28]. In practice, the principle of this technique is based on the study of an electromagnetic wave at a given frequency ν, transmitted through the studied sample, going across it and reflected by a short circuit at the rear of it. Thus, the value of the reflection coefficient S_{11} measured depends on the dielectric properties of the sample materials. After calibration (using short, open, and load Z_0 = 50 Ω), it is possible to measure S_{11} from the cell containing the sample and the corresponding admittance Y_S (*in S*) is obtained from S_{11} (*without unit*) as follows:

$$Z_0 Y_S = \frac{1-S_{11}}{1+S_{11}} \quad (3)$$

which is directly related to the complex permittivity ε by the following approximate and pedagogic relationship at low frequencies (at high frequencies, *i.e.* above 10^8 Hz, the relationship becomes much more complex [29] for *ex-situ* and *in-situ* [9]; these more complex relationships are then used in this article across the frequency range):

$$Y_S = iC\omega \quad (4)$$

where $C = \varepsilon_0\varepsilon S/d$ (S being the area of the circular inner conductor (3.04 mm in diameter) and *d* the thickness of the sample, as a classical formula for a planar capacitor).

Ex situ measurements of the conductivity were carried out for both series of carbons, CB1 and CB2. Conductivities of dry CB1 composite samples were higher than their counterparts CB2 for CB volume fraction above 4.5% (Figure 7a-b). dc-conductivities of the samples with CB1 are easily obtained because the real parts of conductivity are not frequency dependent. On the other hand, conductivities of samples with CB2 are frequency dependent in the higher frequency range (Figure 7a). In this last case, the frequency dependence of the conductivity was previously attributed to space-charge polarization of CB2 clusters (agglomerates). [6] The electronic percolation threshold (*ex situ*) was reached for CB volume content of about 4.5% for the two types of carbon black (Figure 7c). For a dry percolated sample, this shows that a higher specific surface of the additive CB1 has a greater impact on the electronic conductivity by significantly increasing it. Indeed, the greater amount of surface area exposed by the carbon powder results in a thinner thickness of binder deposited on the

surface and between the carbon particles. We mainly focused in the following on electrodes with a CB1 content above this percolation threshold, although it was observed that larger amounts of carbon black increased the brittleness of the sample making it difficult to handle from a practical view point.

In situ measurements were then performed on wet samples to characterize the influence of the electrolyte on electronic transfers in CB1 (as CB2 was previously studied[8]). Figure 7d shows that the conductivity of wet samples with CB1 is lower than that of corresponding dry samples above the percolation threshold. This drop is all the more important as the proportion of CB1 increases. This same trend was previously observed for samples containing CB2 [6]. Moreover, the presence of electrolyte also greatly transforms the real part ε' of the permittivity, especially at higher frequencies where it tends to be negative *(see Supporting Information S1)*. On the other hand, the higher values of ε' at lower frequencies are due to the presence of the electrolyte given the existence of polarizations caused by ion motions and ionic double-layer capacitances *(see Supporting Information S1)*. Moreover, the dielectric spectra are composed of different relaxations induced by charge carrier motions in conducting materials. These relaxations are due to the existence of interfaces (e.g. sample/current collector, cluster/cluster, particle/particle in CB) giving rise to associated space-charges. It results contact resistances, which limit the charge transfers at the different size scales of the samples. Nyquist plots of complex permittivity (ε'' vs. ε') are relevant to highlight the different space-charge relaxations by decomposing the spectra with a homemade software. Dielectric relaxation intensities and frequencies give generally access to space-charge capacitances and charge carriers mobilities, respectively. Nyquist plots of complex resistivity (ρ'' vs. ρ') and conductivity (σ'' vs. σ') are suitable to determine dc-conductivities of the samples and the CB clusters by decomposing the spectra given the presence of multiple interfaces.

The Nyquist plots of complex permittivity (ε'' vs. ε') for the different wet samples (i.e. with CB1 volume content of 5.3%, 6.9%, 7.8% and 9.2%) are shown in Figure 8. The dielectric spectra are decomposed into two contributions P1 and P2. The low-frequency part (P1) of each starting spectrum is well fitted by a quasi-vertical straight line corresponding to the contribution $A(i\omega)^{s-1}$ with *s* here less than 0.06. This response is due either to a more or less disordered long-range conductive network or to distributions of contact resistances and capacitances caused by metallization and electrolyte (see further). By subtracting the P1

contribution, a circular arc highlights a dielectric relaxation (P2 contribution) accurately fitted by a Cole-Cole given by

$$\varepsilon(\omega) = \varepsilon_{hf} + \frac{\varepsilon_{s-}\varepsilon_{hf}}{(1+i\omega\tau_2)^{1-\alpha_2}} \quad (5)$$

where ε_s is the static permittivity of the sample, ε_{hf} the sample background (or higher frequency) permittivity, τ_2 the relaxation time and α a fitting parameter ($0 < \alpha_2 < 1$). The relaxation frequency of P2 is given as $\nu_2 = (2\pi\tau_2)^{-1}$ and $\Delta\varepsilon_2 = (\varepsilon_s - \varepsilon_{hf})$ is the dielectric strength of the relaxation. This type of relaxation is not evidenced for the dry samples, because it might appear beyond the frequency band used here (i.e. $\nu >> 10^{10}$ Hz). The fitting parameters α_2 are 0.18, 0.18, 0.02 and 0.23 for respective CB1 volume contents of 5.3%, 6.9%, 7.8% and 9.2%. Variations of ν_2, $\Delta\varepsilon_2$ and ε_{hf} with CB1 content are shown in Figures 9a, 9b and 9c, respectively. The evolution of ν_2, $\Delta\varepsilon_2$ and ε_{hf} as function of the CB1 content ϕ_{CB} is not monotonic. Indeed, ν_2 and ε_{hf} go through minimum values for 6.9% < ϕ_{CB} < 7.8% while $\Delta\varepsilon_2$ goes through a maximum value for the same ϕ_{CB} content. A transition in the electrical properties of soaked samples is evidenced because of the presence of the electrolyte, and the interactions between the carbon black CB1 and the electrolyte species. These interactions are certainly due the influence of the adsorbed species on the electrical properties of CB1. Figure 9a shows that the relaxation frequencies ν_2 for ϕ_{CB} = 5.3%, 7.8% and 9.2% ($10^9 < \nu_2 < 10^{10}$ Hz) are of the same order of magnitude as that of the dipolar rotation of the solvent EC: DMC which takes place at 6×10^9 Hz at room temperature. There is an exception for ϕ_{CB} = 5.3% where ν_2 is roughly one order of magnitude lower at room temperature (i.e. $\nu_2 = 2.2\text{x}10^8$ Hz). However, it seems unlikely to admit such a variation in the relaxation frequency of the solvent molecules with the CB1 content. One has to wonder why these movements are not highlighted. Indeed, the electrolyte is shunted by the percolated network of CB because of the high electronic conductivity of the latter. The P2 relaxation would then be due to the polarization of the CB1 clusters, which is made possible thanks to the formation of an electronic space charge whose capacitance $C_{sc} \propto \Delta\varepsilon_2 \propto w^{-1}$ where w stands for the space-charge layer thickness [10,30,31]. This fast relaxation would be thus correlated to electronic motions within CB1 clusters. This hypothesis is supported by permittivities of the wet samples lower than that of the corresponding dry samples, which shows that the solvent has no influence on their values for frequencies above 10^8 - 10^9 Hz (Figures 9d-e and Figures S1a-b). Otherwise, the presence of the solvent should have increased the permittivity of the samples, if the CB1 had not shunted

it. The background permittivity ε_{hf} of the wet samples, which is a function of those of γ-alumina (ε = 8.48 [32]), PVdF-HFP ($\varepsilon \approx 10$ at 500 Hz [33]), carbon black CB1 and electrolyte ($\varepsilon \approx 40$ [34]), is negative (Figure 9a). Taking these permittivity values into account, it is very likely that the intrinsic permittivity of CB1 is more negative than the background permittivity ε_{hf} of the wet samples. This result is consistent with the Drude model for the permittivity of the (quasi-) metallic compounds [35]. The high frequency permittivity of the dry samples (Figure 9d-e and Figure S1) is not negative since it is between 10 and 20. Since the dry samples are more conducting than the wet samples, their permittivity could become negative in microwave and terahertz frequency range as for some composite materials containing carbon black (carbon black / polymer mixtures and composite electrodes of carbon black / LiV_3O_8 / PMMA) [24,36]. The observed transition of the dielectric properties of CB1 (for 6.9% < ϕ_{CB} < 7.8%) could be largely due to competitive adsorption of ions (Li^+ and PF_6^-) between alumina and carbon black as for CB2 [6]. This type of transition was previously evidenced for a CB2 volume content $\phi_{CB} \approx$ 7.5% [6]. A surface charge reversal of the interface between CB2 and electrolyte (LP30) was at the origin of this transition [6]. This phenomenon can be understood by the evolution of the surface potential $\Delta\psi$ which is often given by

$$\Delta\psi = \Delta\psi_{ion} + \Delta\psi_{dipole} \quad (6)$$

where $\Delta\psi_{ion}$ is the potential created by adsorbed ions and $\Delta\psi_{dipole}$ the potential due to surface dipoles. A zero-charge interface (zci) was set at the threshold $\phi_{CB} \approx 7.5\%$ due to an equal number of adsorbed Li^+ and PF_6^- at the CB2 surface [6]. The potential is only due to surface dipoles at zci, where $\Delta\psi = \Delta\psi_{dipole}$, since $\Delta\psi_{ion} = 0$. The PVdF-HFP can be present on the surface of the CB and interact with the CB via its dipoles. Indeed, the PVdF – Graphite interactions are between the fluorine atoms (electron attractor) of the PVdF and the surface of the graphite. Indeed, the PVdF – Graphite interactions are between the fluorine atoms (electron attractor) of the PVdF and the surface of the graphite. Two types of dipoles interact thus with the CB surface at the zci: solvent dipoles (EC:DMC) and dipolar species of the PVdF-HFP. Below the zci PF_6^- ions are preferentially adsorbed on CB, while above Li^+ ions become preferentially adsorbed on CB. Due to the neutral nature of the surface at the zci, only dipolar species modify the conductivity of the electrode as compare to the dry electrode. The surface of the CB plays a determining role in the interactions with ions and dipoles which directly influence the electronic conductivity of the carbon and therefore the performance of the Li-

ion battery[37,38]. At a higher CB content, the PVdF-HFP is not present in sufficient quantity: the electrolyte and therefore the Li^+ ions have direct access to the surface of the CB. To support this hypothesis, a NMR study of G. M. Palmer[39] had previously shown preferential adsorption of Li^+ ions at the alumina surface because of their strong bond to the electron donating oxygen basic surface sites. Consequently, the actual transition observed for CB1 would be due to a surface charge reversal of the CB1 / electrolyte interface around the volume content as for CB2. This phenomenon will be hereafter supported by the following data of the conductivity of wet CB1 samples.

Nyquist plots of complex resistivity (ρ'' vs. ρ') and conductivity (σ'' vs. σ') of wet CB1 samples from 10^6 to 10^{10} Hz at room temperature are shown in Figure 10. Complex resistivity plots for ϕ_{CB} = 5.3 and 9.2% (Figures 10a-b) show only one relaxation (circular arc) for each compound. This relaxation is the result of contact resistances and capacitances between the different CB1 clusters. The circular arcs intersect the ρ' axis at ρ_s (*low-frequency side*) and ρ_c (*high-frequency side*), which are respectively sample and CB cluster resistivities (Figures 10a-b). Their corresponding conductivities are thus given by $\sigma_s = \rho_s^{-1}$ and $\sigma_c = \rho_c^{-1}$ at room temperature. Complex conductivity plots for ϕ_{CB} = 6.9 and 7.8% (Fig. 11c-d) highlight some relaxations *(circular arcs)* below 10^8-10^9 Hz and the contributions *(vertical straight lines)* of the negative residual permittivities ε_{hf} above 10^8-10^9 Hz (Figures 10c-d). The relaxations *(circular arcs)* at 5.7×10^6 Hz and 5.7×10^8 Hz would be due to the existence of contact resistances between CB1 samples and the gold film on their surfaces. High-frequency parts of the circular arcs intersect the σ' axis at σ_s *(sample conductivities)*. The straight lines intersect the σ' axis at σ_c *(CB cluster conductivities)* and therefore determine the CB cluster contribution to the complex conductivity, $\sigma(\omega) = \sigma_c + i\omega\varepsilon_0\varepsilon_{hf}$. The conductivities of dry and wet samples have completely different behaviours depending on the CB1 content. The conductivity of dry samples is a regular increasing function of the CB1 content, while that of wet samples increases, reaches a maximum (≈ 7.2%) and then decreases when this content increases (Figure 11a). The impregnation of the solid sample by the liquid electrolyte led thus to an overall reduced conductivity as previously observed for CB2 [6]. Note that the conductivity of the wet samples made with CB2 remained an increasing function of CB2 content [6]. Regarding the impregnation kinetics some studies have shown that a poor wettability leads to increased ionic resistance and inhomogeneous lithium intercalation in the active material. The

electrolyte is supposed to fully fill the electrode pores, as typically assumed in the literature[40]. Below the percolation threshold, the conductivity of the sample with CB2 was increased due to the ionic conductivity of the electrolyte within the pores network [6]. However, beyond the electronic percolation threshold, the decrease in conductivity can be explained as a result of stronger interactions between charge carriers of CB *(electrons and holes)* and adsorbed species of the electrolyte *(PVdF HFP and solvent dipoles, Li^+ and PF_6^- ions)*. The difference in behaviour between wet samples with CB1 and CB2 would be explained by the larger specific area of CB1, hence a stronger interaction with the adsorbed ions. Moreover, that this increase in interactions could be attributed to the relative decrease in the PVdF-HFP content (the ratio of PVdF-HFP volume/CB surface) which makes the CB surface more accessible to the electrolyte, i.e. to the adsorption of Li^+. The evolution of the cluster conductivity σ_c according to ϕ_{CB} shows two linear trends (passing through the origin) on either side of the zci at $\phi_{CB} \approx$ 7.3% (Figure 11b). The evolution of σ_c / ϕ_{CB} according to ϕ_{CB} (Figure 11c) justifies this linear behaviour with a slightly higher slope for ϕ_{CB} = 5.3 and 6.9% than for ϕ_{CB} = 7.8 and 9.2%. The ratio of the slopes is equal to 1.3. In order understand this trend, we recall that the CB clusters are agglomerates of spherical particles in which the graphite layers make them sufficiently conductive. The graphite is known as a compensated semi-metal with an equal number of electrons and holes. It can be either n or p type conductor according to the type of doping [41,42]. The conductivity of the graphite can be thus given by

$$\sigma = \frac{Ne^2\tau_s}{m^*} \tag{7}$$

where τ_s is the scattering time, N the number of charge carriers/unit volume, e = 1.6×10^{-19} C the electronic charge and m* the effective mass of charge carriers (*electrons, holes*). [34, 35] m* is either the hole effective mass $m_h^* = 0.039m_e$ or the electron effective mass $m_e^* = 0.054m_e$ where $m_e \approx 9.11\times10^{-31}$ kg is the electron mass [34, 35]. Note that the graphite conductivity is not achievable by BDS due to its very high value approximating it to a short circuit in the device. By analogy, the CB1 cluster conductivity can be described by a similar expression than (6) with much lower values of N and τ_s due the existence of particle boundaries limiting both the number of mobile charge carriers and their mobility. Assuming that N is proportional to ϕ_{CB}, Eq. (6) becomes

$$\sigma_c = \frac{B}{m^*}\phi_{CB} \tag{8}$$

with B a constant proportional to $e^2\tau_s$. If the transition at $\phi_{CB} \approx 7.3\%$ corresponds to the passage from a p-type *(ϕ_{CB} = 5.3 and 6.9%)* to an n-type *(ϕ_{CB} = 7.8 and 9.2%)* conduction, Eq. (7) gives a slope ratio $m_e^*/ m_h^* = 1.4$ which is very close to experimental value 1.3 of Figure 11c. The assumption that scattering time τ_s is constant (see Eq. 7) is therefore validated in Figure 11d by plotting B/m_e as a function of ϕ_{CB} and using m_h^* and m_e^* below and above the transition, respectively. The fact that the time is short and independent of ϕ_{CB} shows that it would depend only on the CB1 nanostructure especially because of the presence of numerous interfaces (i.e. interparticles, interclusters) thus increasing the frequency of the collisions between the charge carriers. The conductivity of the cluster is mostly performed in the surface layer due to the charge excess (electrons or holes) in the space charge region. The Li^+ or PF_6^- ions adsorbed on the CB surface induce an electric field which can make the graphite (so CB) either n (electron) or p (hole) conductor due to its amphoteric nature (Figure 12a). When the majority of the adsorbed ions are anions (PF_6^-), there is an electron depletion layer leading to excess holes into this surface (space charge) layer (Figure 12a). Otherwise, when the majority of the adsorbed ions are cations (Li^+), a hole depletion layer is established leading to excess electrons in this surface (space charge) layer (Figure 12a). Figure 12b clearly shows that the ratio σ_s / σ_c vs ϕ_{CB} tends towards 1 (i.e. $\sigma_s \approx \sigma_c$) near of the transition. Charge carriers migrate more easily from one cluster to another when the surface is electrically neutral. When the surface is electrically neutral (i.e. at the zci), the interaction between either holes or electrons and ion counterpart does not occur anymore. Indeed, the passage from a cluster to another is facilitated due to the neutral surface because the coulombic interactions do not exist in this case. If there was no dipole, the conductivity would equal that of the dry material. On either side of this transition, the surface conduction is then favored. As shown in Figure 9b, the evolution of $\Delta\varepsilon_2$ as a function of ϕ_{CB} can be explained from the Mott-Schottky relation, which gives the thickness w of the space-charge (depletion) layer capacitance C_{sc} vs. the surface potential $\Delta\psi$, i.e. $w \propto (e.\Delta\psi)^{1/2}$. When the surface charge is zero at the zci *(for ϕ_{CB} = 7.3%)*, the potential $\Delta\psi$ reaches a minimum value because it is only due to adsorbed dipoles ($\Delta\psi_{ion} = 0$). This explains the maximum value of $\Delta\varepsilon_2 \propto w^{-1}$ at the zci for the CB1 volume fraction $\phi_{CB} = 7.3\%$ and the transition from a p-type to a n-type surface conduction at microscopic scale of CB1 clusters (or agglomerates).

Finally, in order to show the complementarity of EIS and BDS, the BDS data should be compared with those of the EIS *(for samples with CB1)* although there is no overlap of their frequency windows. Conductivity values σ'_{50kHz} and σ'_{1mHz} obtained by EIS at respective frequencies 50 kHz and 1 mHz and detailed in Supporting Information S2 are plotted in Figure 12c. They are compared in Fig 13c to the conductivity value σ'_{1MHz} measured by BDS at 1 MHz *(see Figure 7d)* and to that of the sample σ_S obtained from dielectric spectra decomposition *(see Figures 10 and 11a)*. The results show that the global conductivity σ'_{1mHz} is lower by about two orders of magnitude than the sample conductivity σ_S (Figure 12c). This difference between σ'_{1mHz} and σ_S results from the existence of a high interfacial resistance that would be attributed to the barrier created by the adsorbed ions forming a double layer and/or to a hypothetical very thin SEI layer partially covering the carbon black. At the opposite end of the EIS spectra, the conductivity σ'_{50kHz} is close to σ_S for ϕ_{CB} = 9.2 %, while it is less than σ_S by almost an order of magnitude for the smaller CB1 fractions of CB1. Hence, the difference between σ'_{50kHz} and σ_S would be due to the direct contact resistance between the sample and the current collector because of the existence of an insulating gap *(PVdF-HFP and/or γAl_2O_3)* between them. This later contact resistance would become smaller beyond 9% of CB, content for which the contact between the current collector and the sample would be most favorable to the electronic transfer. EIS is more suitable for the study of ionic diffusion and the various contact resistances at the macroscopic scale. On the other hand, the BDS here allows the comprehensive study of carbon black conductivity and permittivity and thus to highlight the influence of the liquid electrolyte on these two parameters.

4. Conclusions

This study establishes a link between the complex hierarchical geometry of carbon black-based composites (such as electrodes of Li-ion batteries) and subsequent limitations of the charge transport occurring at different scales. We substituted the common active material by an insulating compound to specifically highlight the interactions taking place at the liquid electrolyte/carbon black interface. We demonstrated that the carbon specific surface area, as well as its loading, provide an important impedance contribution and play a key role in the electronic percolation threshold, the contact resistance, the SEI formation, and the mass transport efficiency. Most importantly, we revealed an evolution of the electrical conductivity

between the dry and the wet states, which can be attributed to the adsorptions of the electrolyte salt species (Li^+ cation and PF_6^- anion). This phenomenon creates an electrostatic double-layer at the interface between the carbon black and the electrolyte that perturbs the electronic transfers between carbon black clusters. Further experiments are now ongoing for determining the equivalent limitations with the active materials commonly used in commercial lithium-ion batteries for mobility applications.

Conflicts of interest

The authors have no conflict of interest to declare.

Acknowledgements

The authors gratefully acknowledge F. Brisset for SEM characterizations. The project was supported by the Labex Charmmmat as part of the “Investissements d’avenir” program (financial funding from the ANR program no. ANR-11-LABX-0039-grant) and the PEPITE ANR project (ANR-15-CE05-0001) that are acknowledged.

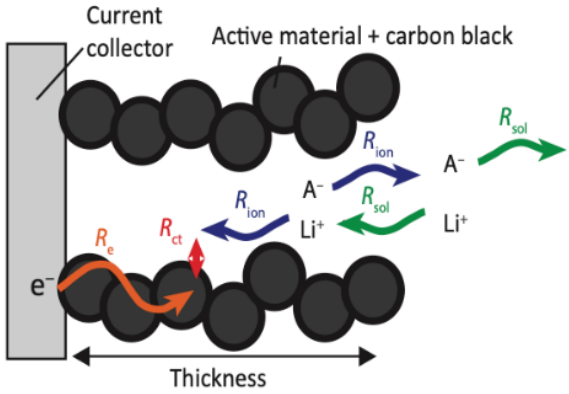

Figure 1. Schematic representation of charge carrier (ion/electron) transport in a hierarchical composite electrode. R_e, R_{ct}, R_{ion} and R_{sol} are related to the resistance of electron within the percolated active material/carbon black network, the charge transfer resistance, the resistance to ionic motion within the electrolyte and solvent resistance, respectively. Li^+ stand for Li ions whereas A^- stands for the counter anion (e.g. PF_6^-). [16]

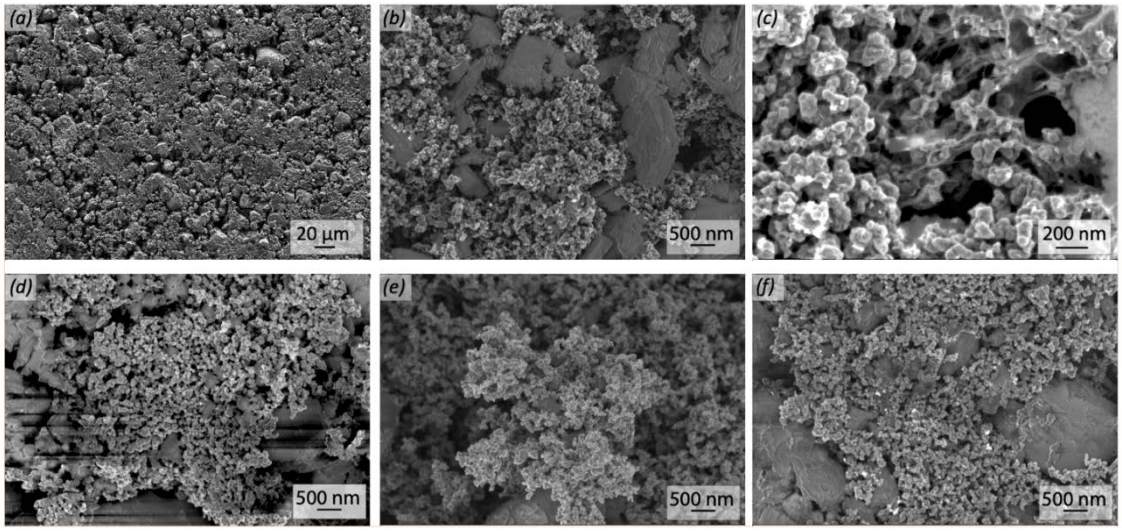

Figure 2. SEM micrographs of γ-Al_2O_3/CB/PB composite samples for different volume contents of carbon black (CB1): (a-c) 5.3 %, (d) 6.9 %), (e) 7.8 %, (f) 9.2 %).

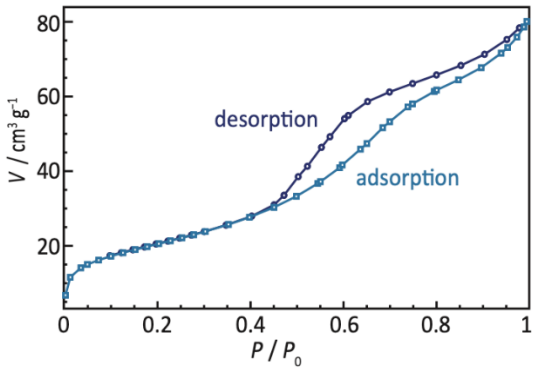

Figure 3. Porosity measurement by BET technique (N_2 adsorption/desorption) of a γ-Al_2O_3/CB1/PB composite electrode. Note that similar isothermal curve shape was observed using CB2.

(a)

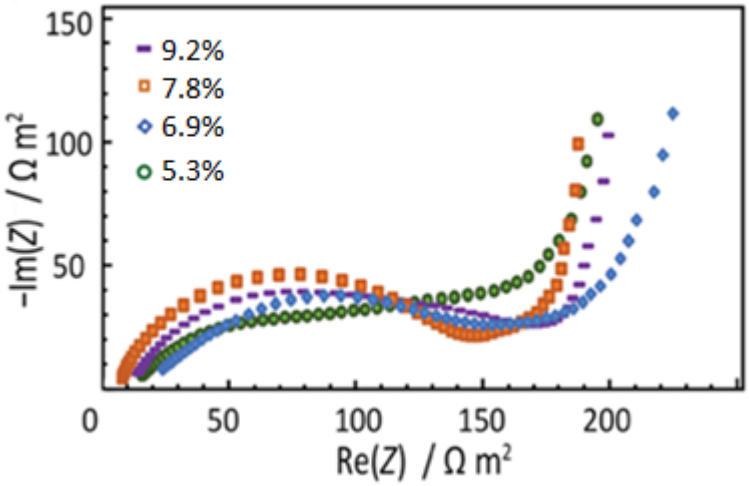

(b)

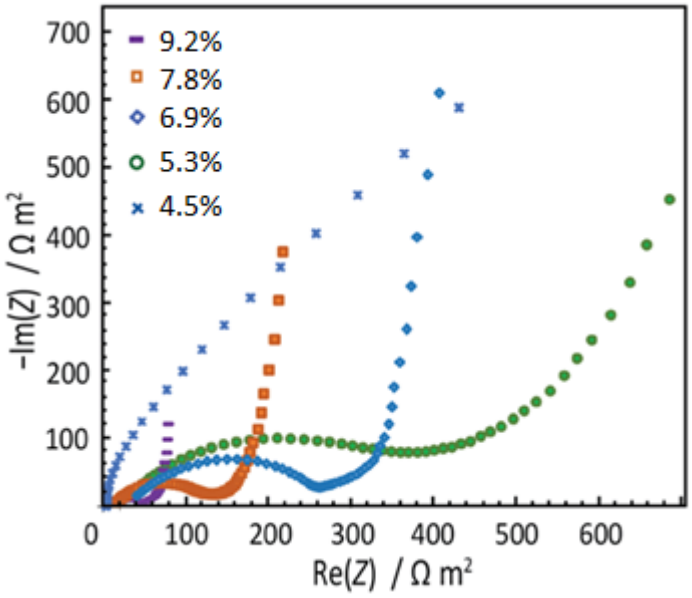

Figure 4. Nyquist diagrams of a γ-Al_2O_3/CB/PB composite material with two different specific surface areas of carbon black: (a) CB1 with 80 $m^2.g^{-1}$ and (b) CB2 with 65 $m^2.g^{-1}$. Studied amounts of carbon black (volume contents): 4.5 %, 5.3 %, 6.9 %, 7.8 % and 9.2 %.

a)

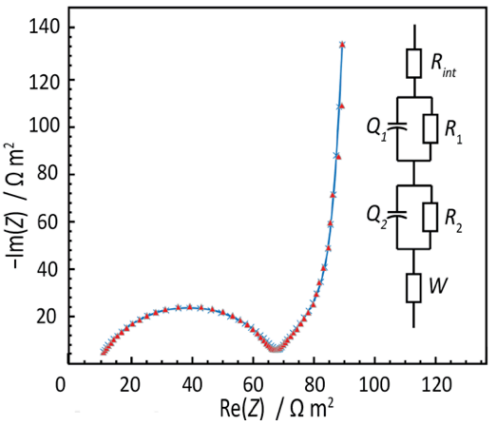

b)

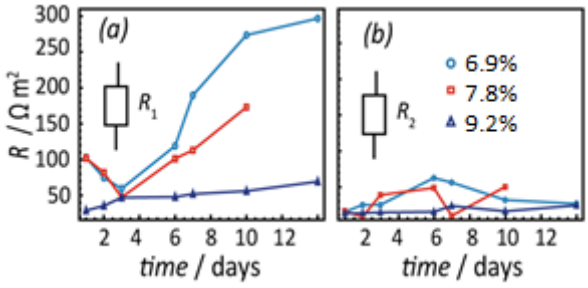

Figure 5. a) Nyquist diagram (red) and corresponding fitting (blue) according to the electrical equivalent circuit shown for a γ-Al_2O_3/CB/PB composite material containing 9.2 % in volume of CB2 (*specific surface area = 65 $m^2.g^{-1}$*). b) Evolution of R_1 (*high frequencies*) and R_2 (*low frequencies*) contributions, respectively, as a function of time with different CB2 volume contents: 6.9 %, 7.8 % and 9.2 %. *W*, *R*, *Q* stands for Warburg element, resistance, and constant phase element of the electrical equivalent circuit modelling the relaxation phenomena in the Nyquist diagram.

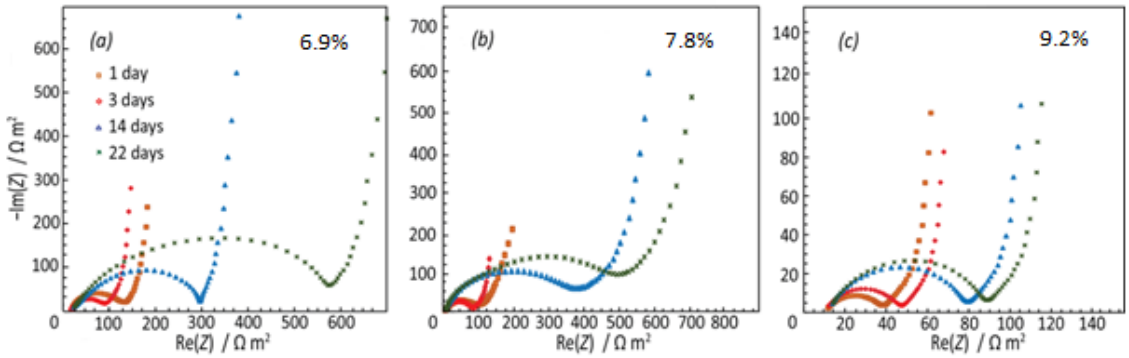

Figure 6. Nyquist diagrams of a γ-Al_2O_3/CB/PB composite material as a function of time (from 1 to 22 days) for different volume contents of carbon black CB2 (*specific surface area = 65 $m^2.g^{-1}$*): (a) 6.9 %, (b) 7.8 %, (c) 9.2 %.

a)

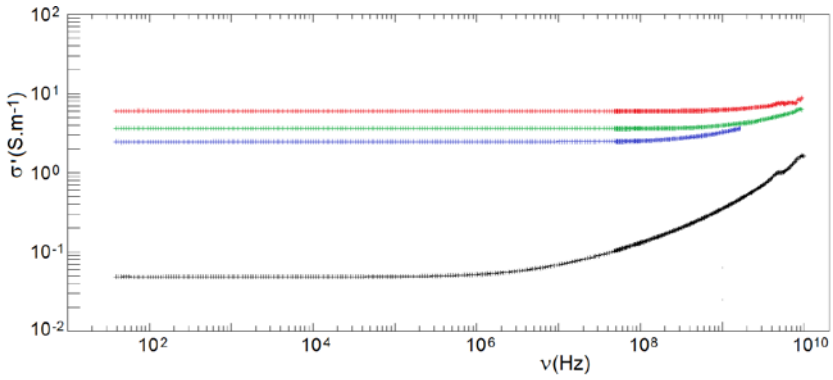

b)

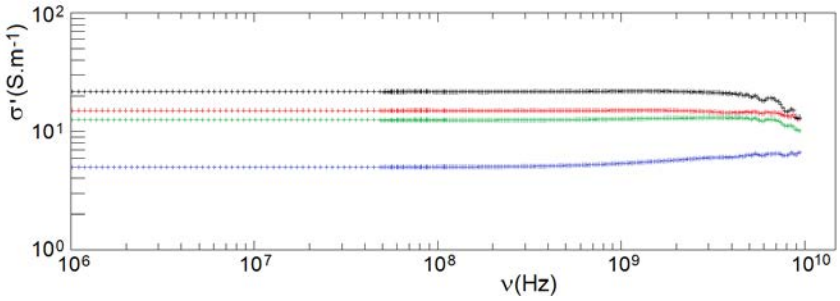

c)

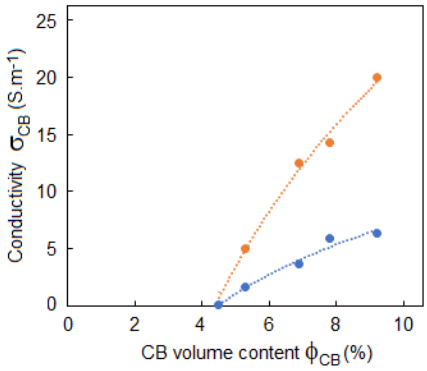

d)

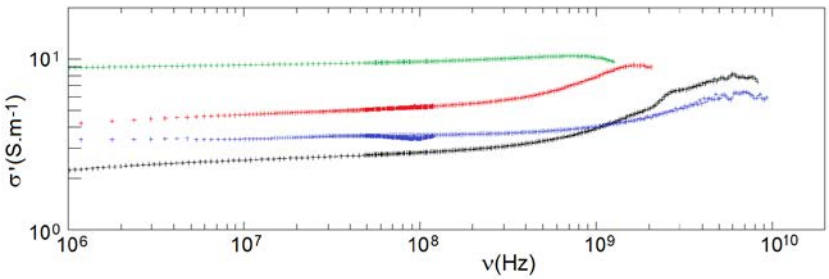

Figure 7. Conductivity as a function of frequency (*ex situ* measurement) of dry samples with two types of carbon black of different volume contents ϕ_{CB}: (a) CB2 (*specific area = 65m²*.g⁻¹) with ϕ_{CB} = 4.5 % (**++**), 5.3 % (++), 6.9 % (++) and 7.8 % (++); (b) CB1 (*specific area = 80 m²*.g⁻¹) with ϕ_{CB} = 5.3 % (++), 6.9 % (++), 7.8 % (++) and 9.2 % (**++**); (c) Dc- conductivity σ_{CB} (*ex situ* measurement) as a function of CB volume content ϕ_{CB} (%) for samples with CB1 (●) and CB2 (●) (*CB percolation threshold* $\phi_c \approx 4.5$ *%*); (d) Conductivity as a function of frequency (*in situ* measurement) of wet samples with CB1 carbon black at different volume contents ϕ_{CB} = 5.3 % (++), 6.9 % (++), 7.8 % (++) and 9.2 % (**++**).

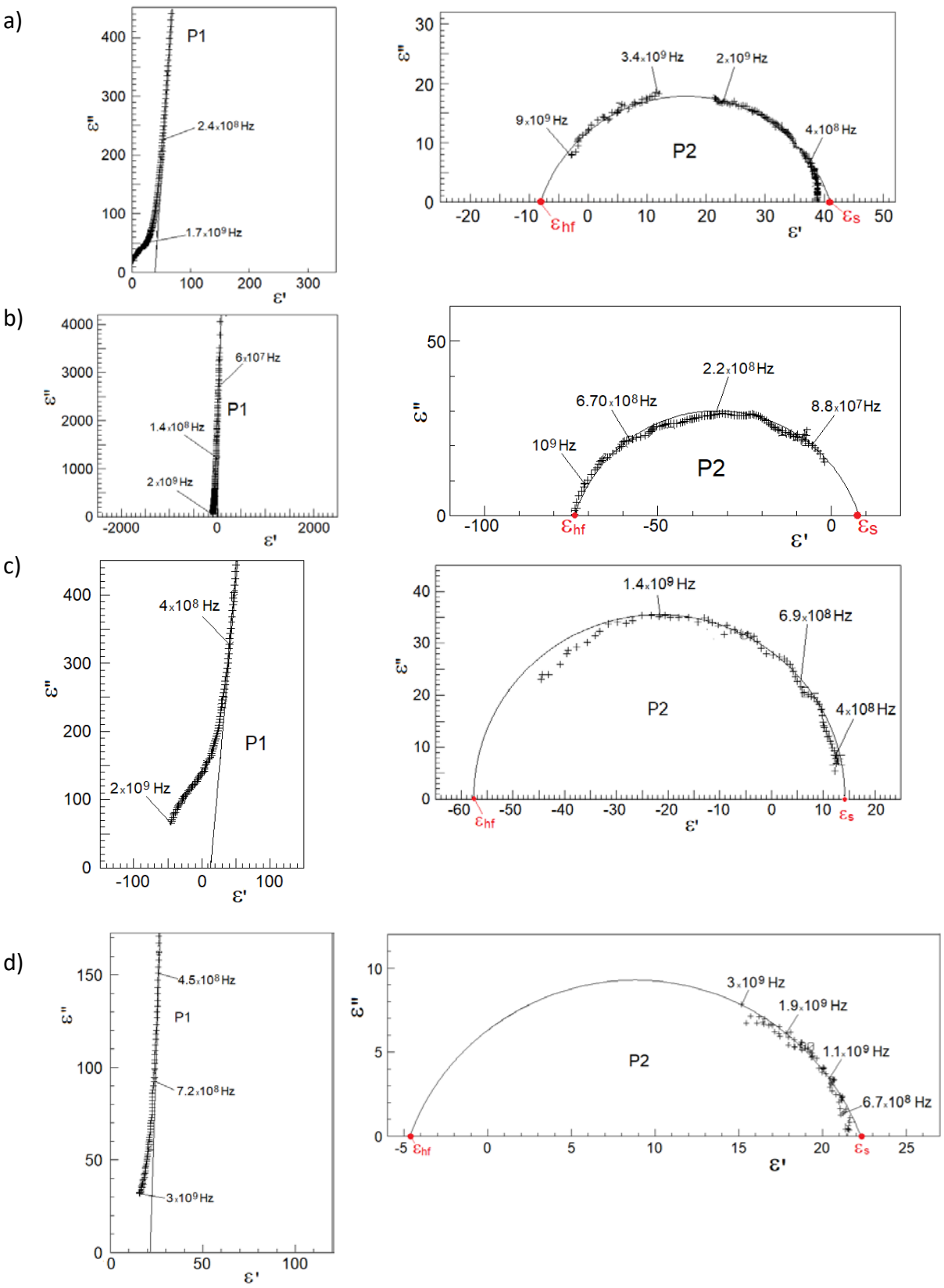

Figure 8. Nyquist plots of complex permittivity (ε" vs. ε') of wet samples at 293 K for CB1 volume contents: a) ϕ_{CB} = 5.3 %, b) ϕ_{CB} = 6.9 %, c) ϕ_{CB} = 7.8 % and d) ϕ_{CB} = 9.2 %. Decomposition of spectra highlights a low-frequency contribution P1 (straight line) and dielectric relaxation P2 (circular arc) obtained upon subtracting P1. ε_s is the static permittivity of the sample and ε_{hf} the background permittivity of the CB1 cluster.

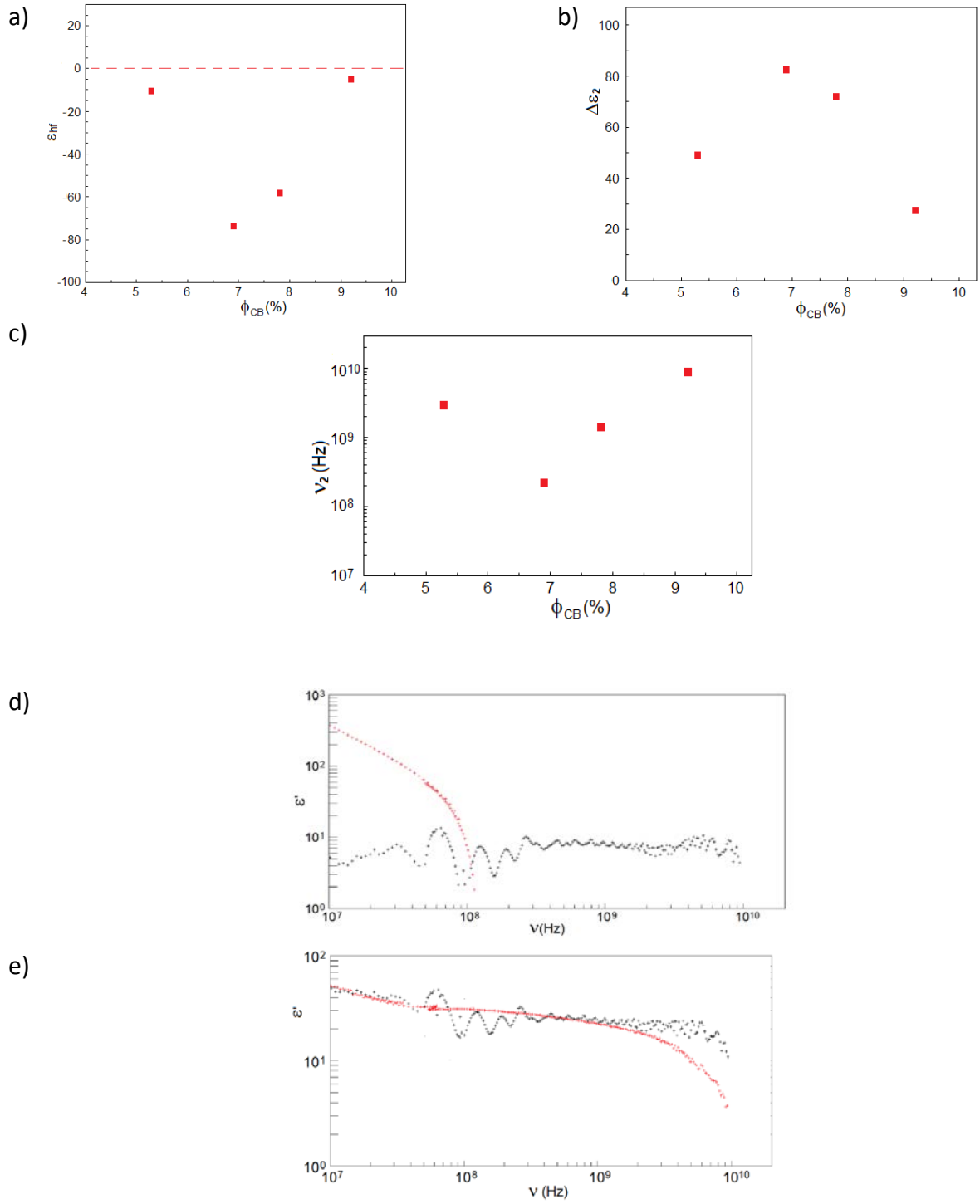

Figure 9. Parameters of dielectric relaxation P2 vs. CB1 volume fraction ϕ_{CB} of wet samples: a) background permittivity ε_{hf}, b) dielectric strength $\Delta\varepsilon_2$, c) relaxation frequency ν_2. Real part ε' of the permittivity vs. frequency ν for dry (++) and wet (++) samples with CB1 volume fraction ϕ_{CB}: d) 6.9 % and e) 9.2 %.

a)

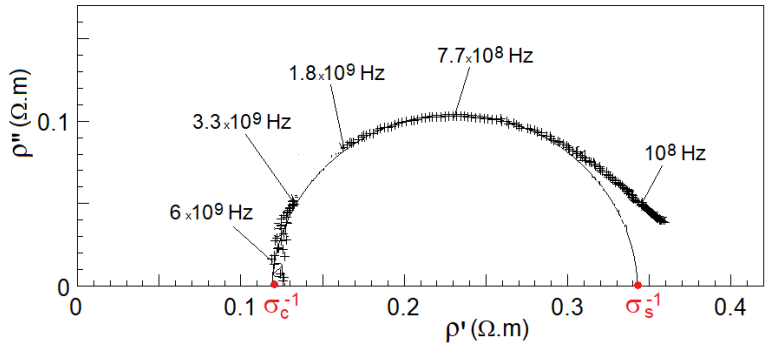

b)

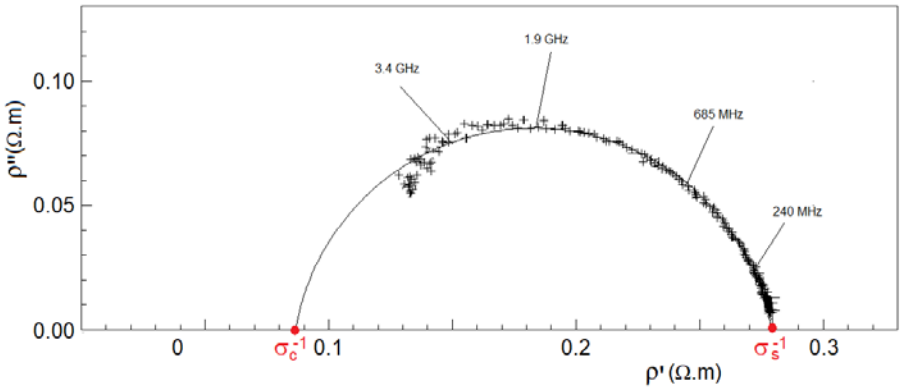

c)

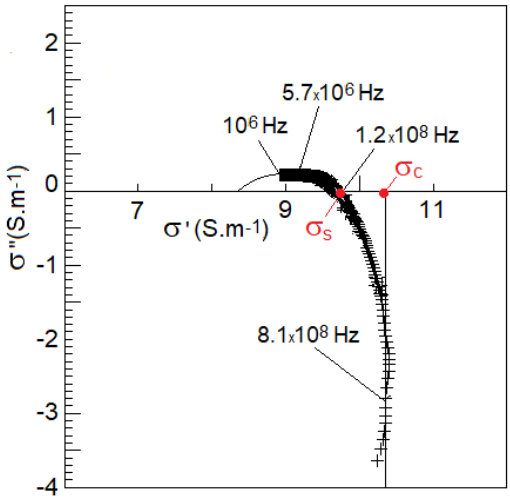

d)

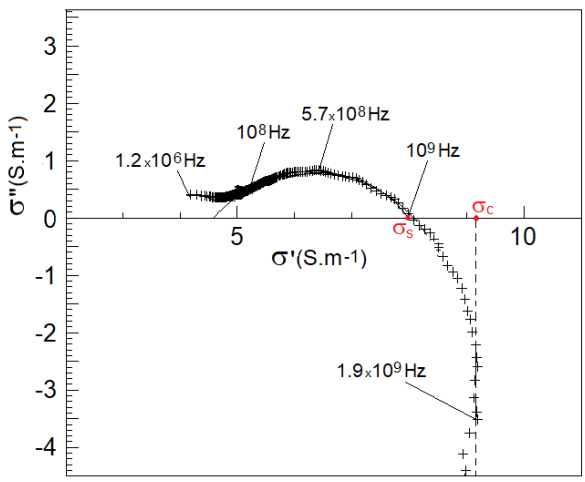

Figure 10. Nyquist plots of complex resistivity (ρ" vs. ρ') of wet samples at 293 K for CB1 volume fraction: a) ϕ_{CB} = 5.3 % and b) ϕ_{CB} = 9.2 %. Nyquist plots of complex conductivity (σ" vs. σ') at 293 K for CB1 volume fraction: c) ϕ_{CB} = 6.9 % and d) ϕ_{CB} = 7.8 %. σ_s and σ_c correspond sample and CB1 cluster conductivities, respectively.

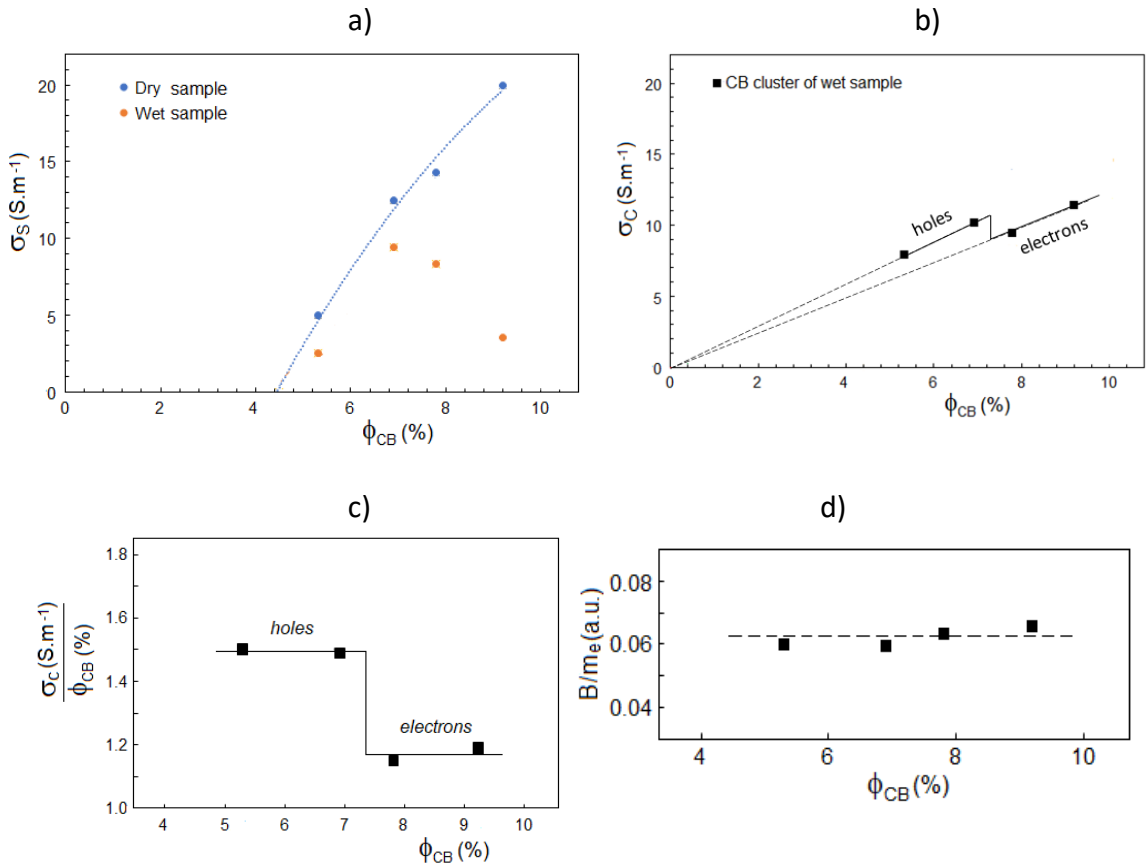

Figure 11. a) Conductivities σ_S of dry (●) and wet (●) samples vs. CB1 volume fraction ϕ_{CB} at 293 K; b) Conductivity σ_C of wet sample vs. CB1 volume fraction ϕ_{CB} at 293 K; c) Ratio σ_C / ϕ_{CB} vs. CB1 volume fraction ϕ_{CB} at 293 K; d) B/m_e vs. CB1 volume fraction ϕ_{CB} at 293 K. $\frac{B}{m_e} = \frac{\sigma_C}{\phi_{CB}} \frac{m*}{m_e}$ where $m_e \approx 9.11\times10^{-31}$ kg is the electron mass and m* the effective mass of holes ($m^* = m_h^* = 0.039m_e$) or electrons ($m^* = m_e^* = 0.054m_e$). B/m_e is calculated using m_h^* for ϕ_{CB} = 5.3 and 6.9 % and m_e^* for ϕ_{CB} = 7.8 and 9.2 %.

a)

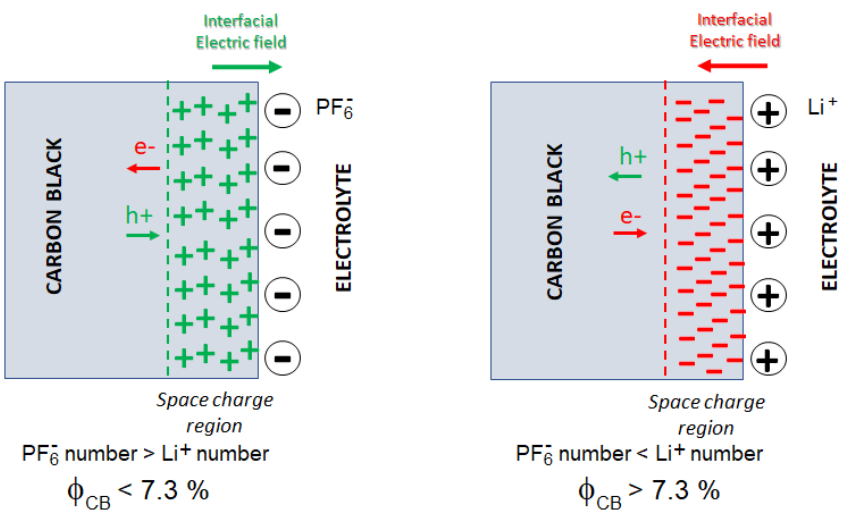

b)

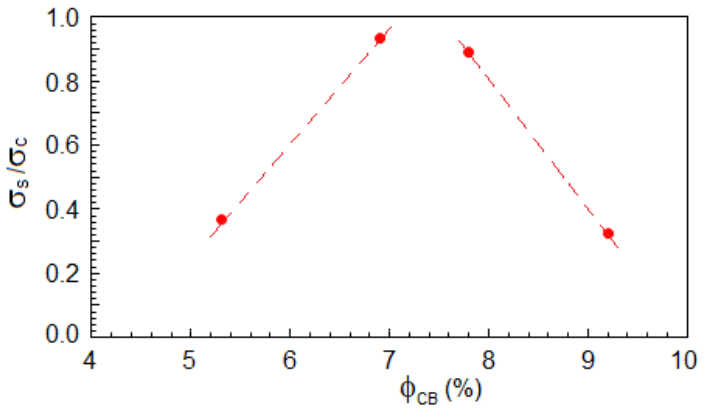

c)

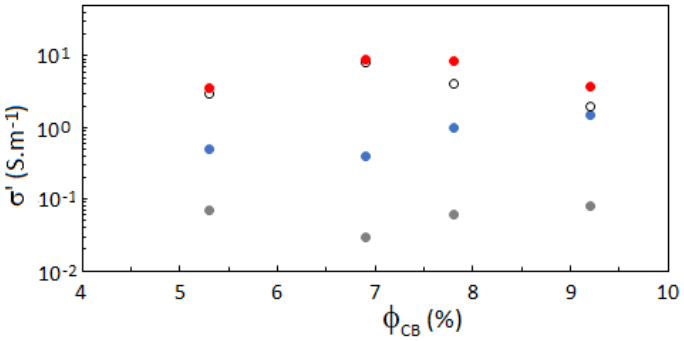

Figure 12. a) Modification of the sign of space charge layer at the carbon black (CB1) surface as function of the CB1 volume fraction ϕ_{CB}: left hand figure (majority of adsorbed PF_6^- anions resulting in an electron depletion layer with excess holes) and right hand figure (majority of adsorbed Li^+ cations resulting in a hole depletion layer with excess electrons); b) Ratio σ_c/σ_s vs. ϕ_{CB} where σ_c and σ_s are conductivities of cluster and sample *(set of CB1 clusters)*, respectively; c) Conductivities (real parts) vs. CB1 volume fraction: σ'_{1mHz} (•) and σ'_{50kHz} (•) obtained by EIS at 1 mHz and 50 kHz *(see Fig. 5a, Supporting Information S2 and Table S1)*, σ'_{1MHz} measured at 1 MHz by BDS (o) (see Fig. 8d), and σ_s (•) *(sample conductivity, see Fig. 11 and 12a)*.

References

1. J.M. Tarascon and M. Armand. Issues and challenges facing rechargeable lithium batteries, Nature 414 (2001) 359-367.

2. D.P. Singh, F.M. Mulder, A.M. Abdelkader and M. Wagemaker. Facile Micro Templating $LiFePO_4$ Electrodes for High Performance Li-ion Batteries, Adv. Energy Mater. 3 (2013) 572-578.

3. J. Liu, H. Yuan, X. Tao, Y. Liang, S. Jae Yang, J.-Q. Huang, T.-Q. Yuan, M.-M. Titirici, and Q. Zhang, Recent progress on biomass-derived ecomaterials toward advanced rechargeable lithium batteries, EcoMat 2 (2020), e12019.

4. X. Liu, X. Li, Y. Li, H. Zhang, Q. Jia, S. Zhang, and W. Lei, High-entropy oxide: A future anode contender for lithium-ion battery (2022), e12261.

5. B. Dunn, H. Kamath and J.M. Tarascon. Electrical Energy Storage for the Grid: A Battery of Choices, Science 334 (2011) 928-935.

6. M. Osiak, H. Geaney, E. Armstrong and C. O'Dwyer. Structuring materials for lithium-ion batteries: advancements in nanomaterial structure, composition, and defined assembly on cell performance, J. Mater. Chem. A 2 (2014) 9433-9460.

7. J.C. Badot, E. Ligneel, O. Dubrunfaut, D. Guyomard and B. Lestriez. A multiscale description of the electronic transport within the hierarchical architecture of a composite electrode for lithium batteries, Adv. Funct. Mater. 19 (2009) 1-10.

8. E. Panabière, J.C. Badot, O. Dubrunfaut, A. Etiemble and B. Lestriez. Electronic and Ionic Dynamics Coupled at Solid-Liquid Electrolyte Interfaces in Porous Nanocomposites of Carbon Black, Poly(vinylidene fluoride), and γ-Alumina, J. Phys. Chem. C 121 (2017) 8364-8377.

9. M. D. Levi and D. Aurbach. Impedance of a Single Intercalation Particle and of Non-Homogeneous, Multi-layered Porous Composite Electrodes for Li-ion Batteries, J. Phys. Chem. B 108 (2004) 11693-11703.

10. C. Fongy, A.C. Gaillot, S. Jouanneau, D. Guyomard and B. Lestriez. Ionic vs Electronic Power Limitations and Analysis of the Fraction of Wired Grains in $LiFePO_4$ Composite Electrodes, J. Electrochem. Soc. 157 (2010) A885-A891.

11. K.A. Seid, J.C. Badot, C. Perca, O. Dubrunfaut, P. Soudan, D. Guyomard and B. Lestriez. An in situ multiscale study of ion and electron motion in a lithium-ion battery composite electrode. Adv. Energy Mater. 2015, 5, 1-10.

12. A. Agrawal, O. Dubrunfaut, L. Assaud, S. Franger, B. Lestriez, J.C. Badot. Influence of a Liquid Electrolyte on Electronic and Ionic Transfers in $LiNi_{0.5}Mn_{0.3}Co_{0.2}O_2$ / Poly(vinylidene

fluoride-co-hexafluoropropylene) based Composite Material, J. Phys. Chem. C 125 (2021) 17629-17646.

13. Siroma, Z.; Hagiwara, J.; Yasuda, K.; Inaba, M.; Tasaka, A. Simultaneous Measurement of the Effective Ionic Conductivity and Effective Electronic Conductivity in a Porous Electrode Film Impregnated with Electrolyte, J. Electroanal. Chem. 648 (2010) 92−97.

14. S. W. Peterson, D. R. Wheeler, Direct Measurements of Effective Electronic Transport in Porous Li-Ion Electrodes, J. Electrochem. Soc. 161 (2014) A2175−A2181

15. K.A. Seid, J.C. Badot, O. Dubrunfaut, M.T. Caldes, N. Stephant, L. Gautier, D. Guyomard and B. Lestriez. Multiscale electronic transport in $Li_{1+x}Ni_{1/3-u}Co_{1/3-v}Mn_{1/3-w}O_2$: a broadband dielectric study from 40 Hz to 10 GHz, Phys. Chem. Chem. Phys. 15 (2013) 19790-19798.

16. K.A. Seid, J.C. Badot, O. Dubrunfaut, S. Levasseur, D. Guyomard and B. Lestriez. Multiscale electronic transport mechanism and true conductivities in amorphous carbon-$LiFePO_4$ nanocomposites, J. Mater. Chem. 22 (2012) 2641-2649.

17. V.A. Agubra, and J.W. Fergus. The formation and stability of the solid electrolyte interface on the graphite anode, J. Power Sources 268 (2014) 153-162.

18. J. Illig, M. Ender, T. Chrobak, J. P. Schmidt, D. Klotz and E. Ivers-Tiffée. Separation of Charge Transfer and Contact Resistance in $LiFePO_4$-Cathodes by Impedance Modelling Batteries and Energy Storage, J. Electrochem. Soc. 150 (2012) A952-A960.

19. J.M Atebamba, J. Moskon, S. Pejovnik and M. Gaberscek. On the Interpretation of Measured Impedance Spectra of Insertion Cathodes for Lithium-Ion Batteries and Energy Storage, J. Electrochem. Soc. 157 (2010) A1218-A1228.

20. N. Ogihara, Y. Itou, T. Sasaki, and Y. Takeuchi. Impedance Spectroscopy Characterization of Porous Electrodes under Different Electrode Thickness Using a Symmetric Cell for High-Performance Lithium-Ion Batteries, J. Phys. Chem. C 119 (2015) 4612-4619.

21. E. Radvanyi, W. Porcher, E. De Vito, A. Montani, S. Franger and S. Jouanneau Si Larbi. Failure mechanisms of nano-silicon anodes upon cycling: an electrode porosity evolution model, Phys. Chem. Chem. Phys. 16 (2014) 17142-17153.

22. A. Awarke, M. Wittler, S. Pischinger and J. Bockstette. A 3D Mesoscale Model of the Collector-Electrode Interface in Li-Ion Batteries and Energy Storage, J. Electrochem. Soc. 159 (2012) A798-A808.

23. A. van Bommel and R. Divigalpitiya. Effect of Calendering $LiFePO_4$ Electrodes Batteries and Energy Storage, J. Electrochem. Soc. 159 (2012) A1791-A1795.

24. J-H. Hwang, K.S. Kirkpatrick, T.O. Mason and E.J. Garboczi. Experimental limitations in impedance spectroscopy: Part IV. Electrode contact effects, Solid State Ionics 98 (1997) 93-104.

25. S. Larfaillou, D. Guy-Bouyssou, F. Le Cras, S. Franger. Comprehensive characterization of all-solid-state thin films commercial microbatteries by Electrochemical Impedance Spectroscopy, J. Power Sources 319 (2016) 139-146.

26. S. J. An, J. Li, Claus Daniel, D. Mohanty, S. Nagpure, and D. L. Wood. The state of understanding of the lithium-ion-battery graphite solid electrolyte interphase (SEI) and its relationship to formation cycling, Carbon 105 (2016) 52-76.

27. P. Bernard, H. Martinez, C. Tessier, E. Garitte, S. Franger, and R. Dedryvere. Role of negative electrode porosity in long-term aging of NMC/graphite Li-ion batteries, J. Electrochem. Soc. 162 (2015) A7096-A7103.

28. P.E. Cabelguen, D. Peralta, Mikael Cugnet, J.C. Badot, O. Dubrunfaut, D. Guyomard, and P. Mailley. Rational Analysis of Layered Oxide Power Performance Limitations in a Lithium Battery Application, Adv. Sustainable. Systems. 19 (2017) 1700078.

29. N.E Belhadj-Tahar and A. Fourrier-Lamer. Broad-band analysis of a coaxial discontinuity used for dielectric measurements, IEEE Trans. Microwave Theory Tech. 34 (1986) 346-350.

30 N. Sato. Electrochemistry at Metal and Semiconductor Electrodes; Elsevier, Amsterdam, 1998.

31 H. Gerischer. Advances in Electrochemistry and Electrochemical Engineering, Vol. 1, Eds. Delahay P. and Tobias Ch. W., Interscience Publ., New York 1961.

32. C.K. Lee, E. Cho, H.S Lee, K.S. Seol, S. Han. Comparative of electronic structures and dielectric properties of alumina polymorphs by first-principles methods, Phys. Rev. B 76 (2007) 245110.

33. A.L. Gayen, D. Mondal, D. Roy, P. Bandyopadhyay, S. Manna, R. Basu, S Das, D.S. Bhar, B.K. Paul, P. Nandy. Improvisation of electrical properties of PVDF-HFP: use of novel metallic nanoparticles, J Mater Sci: Mater Electron 28 (2017) 14798.

34. K. Xu. Nonaqueous Liquid Electrolytes for Lithium-Based Rechargeable Batteries. Chem. Rev. 104 (2004) 4303.

35. C.F. Martens, A. Reedijk, H. B. Brom, D. M. de Leeuw, and R. Menon. Metallic state in disordered quasi-one-dimensional conductors, Phys. Rev. B 63 (2001) 073203.

36. M.A. Seo, J.W. Lee, and D.S. Kim. Dielectric constant engineering with polymethylmethacrylate-graphite metastate composites in the terahertz region, J. Appl. Phys. 99 (2006) 066103.

37. J. Lianga, and Q. Yang, Aggregate structure and percolation behavior in polymer/carbon black conductive composites, J. Appl. Phys. 102 (2007), 083508.

38. I. Balberg, A comprehensive picture of the electrical phenomena in carbon black–polymer composites, Carbon 40 (2002), 139.

39. G.M. Palmer. NMR Study of Relaxation and Equilibrium of Lithium Ions in Contact with Alumina, J. Magn. Reason. 11 (1973) 388.

40. A. Shodiev, E. Primo, O. Arcelus, M. Chouchane, M. Osenberg, A. Hilger, I. Manke, J. Li, and A. A. Franco, Insight on electrolyte infiltration of lithium ion battery electrodes by means of a new three-dimensional-resolved lattice Boltzmann model, En. Stor. Mater. 38 (2021), 80.

41. N. Brandt, S. Chudinov, and Y.G. Ponomarev, Semimetals, 1. Graphite and its compounds, North Holland, 1988.

42. J. Schneider, Propriétés électroniques du graphite, Thesis, Université de Grenoble, France, 2010.